Dalton Transactions

PAPER

View Article Online
View Journal

Cite this: DOI: 10.1039/c6dt02740g

Oxalate-mediated long-range antiferromagnetism order in $Fe_2(C_2O_4)_3{\cdot}4H_2O$†

G. Rousse*[a,b,c] and J. Rodríguez-Carvajal[d]

Received 11th July 2016,
Accepted 9th August 2016

DOI: 10.1039/c6dt02740g

www.rsc.org/dalton

In this paper we reveal for the first time the magnetic properties of iron oxalate tetrahydrate, a compound commercialized for decades but whose structure was solved only recently. Susceptibility measurements and neutron powder diffraction experiments reveal the establishment of a long-range magnetic order below 25 K. The magnetic structure can be described with a propagation vector $\mathbf{k} = (\frac{1}{2}, \frac{1}{2}, 0)$. The magnetic ordered phase is characterized by collinear antiferromagnetic couplings between adjacent Fe^{3+} atoms, whatever the chelating mode of the oxalate ligand. Moreover, an analysis of the topology reveals that a fourth Fe–Fe magnetic coupling has to be taken into account to generate 3D long range order.

Introduction

Transition metal (TM) molecular based compounds represent a heavily studied class of compounds because they present many attractive properties such as catalytic activity, storage properties, electric conductivity, non-linear optical properties, *etc.* The choice of the ligand leads to various network topologies and therefore allows tailoring the functionalities of a material.[1–7] Carboxylate ligands such as formate, oxalate, terephthalate, maleate, and malonate groups have been considered and mediated interesting functionalities.[8–12] Their versatility is rich as they can coordinate 3d transition metals in various bridging modes: *syn–syn*, *syn–anti*, and *anti–anti*, through one or both carboxylate groups.[13,14] In particular, carboxylate can mediate significant ferromagnetic or antiferromagnetic interactions between TM,[8,11,12,15–20] leading to properties such as magnetoelectricity and multiferroicity.[10,13,21–24] Oxalate ions, thanks to their bis-chelating coordinating ability, have been largely employed to create two and three dimensional networks with the aim of creating new molecular-based magnets.[25–30] Oxalate groups can indeed mediate significant antiferro- and ferro-magnetic exchange interactions when they bridge magnetic ions, such as 3d transition metals.

In this paper, we focus on iron(III) oxalate tetrahydrate. This compound is mainly used as a catalyst for the photo-reduction/oxidation reactions of dyes, organics wastes, *etc.* Commercialized by Sigma-Aldrich for years, the structure of this compound was solved only recently from combined X-ray and neutron powder diffraction.[31] Moreover, its ability to reversibly insert lithium ions (coupled with a reversible reduction of Fe^{3+} to Fe^{2+}) was shown, so that this compound can serve as a positive electrode material for Li batteries.[31] The network made by Fe atoms and oxalate anions is also likely to generate long-range magnetic interactions. The oxalate groups chelate Fe^{3+} in two different modes: a tetradentate manner and a bidentate manner with oxygen atoms in a *trans* configuration. In the present study, we explore the magnetic behaviour of iron(III) oxalate tetrahydrate using susceptibility measurements, and we show that this compound is antiferromagnetic with the onset of a long range ordering at $T_N = 25$ K. We solve the magnetic structure of $Fe_2(C_2O_4)_3{\cdot}4H_2O$ using neutron powder diffraction, a technique which is still confidential in coordination compounds.[25] Moreover, we examine exchange interactions and geometrical paths through oxalate groups and we discuss the obtained magnetic structure's topology. Overall, $Fe_2(C_2O_4)_3{\cdot}4H_2O$ can be regarded as a model compound for studying oxalate-mediated magnetic interactions. Lastly, the magnetic structure is analysed in terms of symmetry.

Experimental and computational details

X-ray and neutron diffraction

XRD patterns of the as-prepared compounds were recorded using a Bruker D8-Advance Diffractometer with Cu-K_α

[a]UMR 8260, Chimie du Solide et de l'Energie, Collège de France, 11 place Marcelin Berthelot, 75231 Paris Cedex 05, France.
E-mail: gwenaelle.rousse@college-de-france.fr
[b]Réseau sur le Stockage Electrochimique de l'Energie (RS2E), FR CNRS 3459, France
[c]Sorbonne Universités - UPMC Univ Paris 06, 4 place Jussieu, F-75005 Paris, France
[d]Institut Laue Langevin, 71 avenue des Martyrs, CS 20156 - 38042 Grenoble Cedex 9, France

†Electronic supplementary information (ESI) available: Magnetic mCIF file. See DOI: 10.1039/c6dt02740g

radiation (λ_1 = 1.54056 Å, λ_2 = 1.54439 Å) equipped with a LynxEye detector operating at 40 kV and 40 mA.

Neutron patterns were recorded as a function of temperature on the D1B powder diffractometer at Institut Laue Langevin, Grenoble, France. The powdered samples were placed in a vanadium cylindrical container (diameter 8 mm). A wavelength of 2.52 Å obtained from a graphite monochromator was used.

All powder patterns were refined using the Rietveld method[32] as implemented in the FullProf program.[33,34]

Magnetic measurements

Temperature-dependent susceptibility measurements and magnetization curves were carried out using a SQUID (Quantum design), in zero field cooled (ZFC) and field cooled (FC) modes, under an applied magnetic field of 1 kOe. About 20–30 mg of powder was placed into gel caps for the measurement.

Results

Preparation and structural characterization

$Fe_2(C_2O_4)_3{\cdot}4H_2O$ was obtained by precipitation of a 10 ml water solution containing $H_2C_2O_4{\cdot}2H_2O$ and $Fe(NO_3)_3{\cdot}9H_2O$ precursors with a 3 : 2 molar ratio. The glass vial containing the solution was covered with an aluminium foil to prevent the photoreduction in water of the iron(III) oxalate complex into iron(II) oxalate, and complete evaporation in an oil bath at 80 °C under continuous stirring, led to $Fe_2(C_2O_4)_3{\cdot}4H_2O$. The sample used for the present study was thoroughly studied with Mössbauer spectroscopy and DTA measurements and assessed both the oxidation state of iron and the water content, as detailed in our previous paper.[31] Its X-ray powder diffraction (XRD) pattern is analogous to the one produced by commercial "$Fe_2(C_2O_4)_3{\cdot}6H_2O$" powders (Sigma-Aldrich), provided the commercialized compound is preliminarily heated at 150 °C for a few hours to remove possible surface water and kept in an Ar glovebox (we showed in a previous paper that only 4 out of the 6 water molecules declared by the supplier are structural water).[31] The Rietveld refinement confirms the previously reported triclinic structure cell with the lattice parameters: a = 5.306(1) Å, b = 6.637(1) Å, c = 9.138(1) Å, α = 91.79(1)°, β = 97.58(1)° and γ = 93.32(1)° (Fig. 1a).[31]

The structure of $Fe_2(C_2O_4)_3{\cdot}4H_2O$ is shown in Fig. 1b. Iron atoms sit in the middle of an octahedron built on a water molecule and 5 oxygen atoms belonging to three crystallographically distinct C_2O_4 oxalate groups. Each oxalate molecule is placed on an inversion centre of $P\bar{1}$ (origin of the cell, centre of the cell and middle of the (**a**, **b**) face for oxalate groups built on C1, C2 and C3 atoms, respectively). These molecules connect $FeO_5(H_2O)$ octahedra in a tetradentate manner for both of them (O_2–C2–C2–O_2 and O_2–C3–C3–O_2), and in a bidentate manner for the oxalate O_2–C1–C1–O_2. Lastly, a second water molecule is present in the structure. For the sake of clarity, oxygen being part of oxalate molecules is represented in red, while oxygen from water is shown in pink. Orientation of the water molecules, *i.e.* localization of hydrogen atoms was done by neutron diffraction, and revealed the presence of hydrogen bonds that holds the whole structure.[31]

This structure makes $Fe_2(C_2O_4)_3{\cdot}4H_2O$ a model compound for studying the manner carboxylate ligands mediate Fe^{3+} magnetic interactions. This motivated the study of the magnetic properties of this compound.

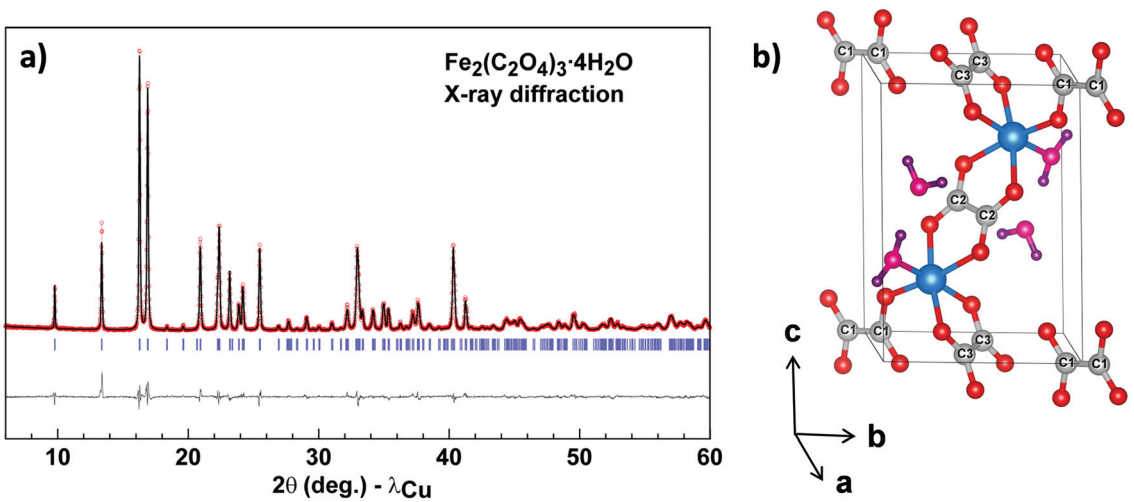

Fig. 1 (a) Rietveld refinement of laboratory X-ray diffraction pattern of $Fe_2(C_2O_4)_3{\cdot}4H_2O$. The red crosses, black continuous line and bottom dark gray line represent the observed, calculated, and difference patterns, respectively. Vertical blue tick bars are the Bragg positions. (b) Structure of $Fe_2(C_2O_4)_3{\cdot}4H_2O$. Iron atoms are shown as blue balls, carbon and oxygen atoms from oxalate ligands are coloured in gray and red, respectively. Oxygen and hydrogen atoms from structural water are coloured in pink and purple, respectively.

Magnetization

The magnetic susceptibility of $Fe_2(C_2O_4)_3{\cdot}4H_2O$, summarized in Fig. 2a and b, can be fitted using the modified Curie–Weiss equation in the high temperature region (200–400 K):

$$\chi = \chi_0 + \frac{C}{T - \theta_{CW}}$$

The χ_0 term (refined value of 0.0004(3) emu mol^{-1} Oe^{-1}) includes a diamagnetic component from the sample holder and core diamagnetism from the compound.

A negative Curie–Weiss temperature (θ_{CW}) of −101(4) K indicates antiferromagnetic (AFM) interactions between Fe^{3+} atoms. The iron effective moment extracted from the Curie constant is 5.88(2)μ_B, in very good agreement with the 5.92μ_B value expected for an isotropic d^5 cation in a regular octahedral environment.[35]

At low temperature, the susceptibility shows a broad maximum around 55 K followed by a decrease when the temperature is cooled down to 2 K. This may be an indication of low-dimensionality short range correlations above three-dimensional (3D) ordering. Note that the zero-field cooled (ZFC) and field-cooled (FC) susceptibilities superimpose down to the lowest measured temperature. Moreover, the $M(H)$ loops measured at 2 K do not present any opening, but rather linear behaviour typical of a fully 3D antiferromagnetic structure (Fig. 2c). To further address the magnetic behaviour of $Fe_2(C_2O_4)_3{\cdot}4H_2O$, we used neutron powder diffraction as a function of temperature.

Magnetic structure determination

$Fe_2(C_2O_4)_3{\cdot}4H_2O$ was studied by means of neutron powder diffraction experiments performed on the D1B instrument at the Institut Laue Langevin. This diffractometer presents a

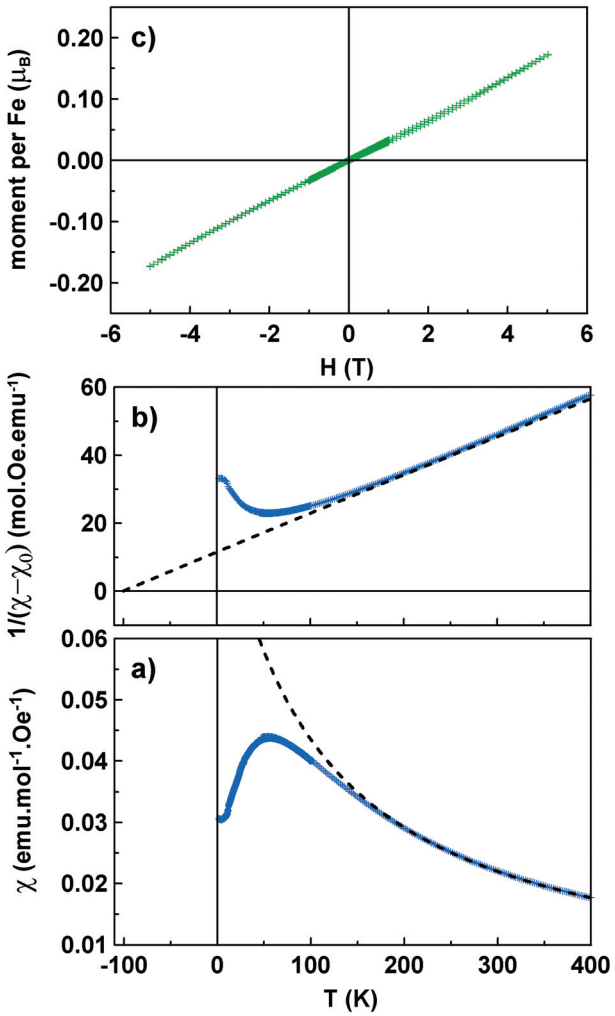

Fig. 2 (a) and (b) Temperature dependence of the magnetic susceptibility χ of $Fe_2(C_2O_4)_3{\cdot}4H_2O$ and its inverse $1/(\chi - \chi_0)$, measured under a field of 1 kOe (field cooled and zero field cooled curves superimpose). The diamagnetic component χ_0 from the sample holder and core diamagnetism has been taken into account for the Curie–Weiss fit, which is shown as a black dashed line. (c) *M versus H* hysteresis loops measured at a temperature of 2 K.

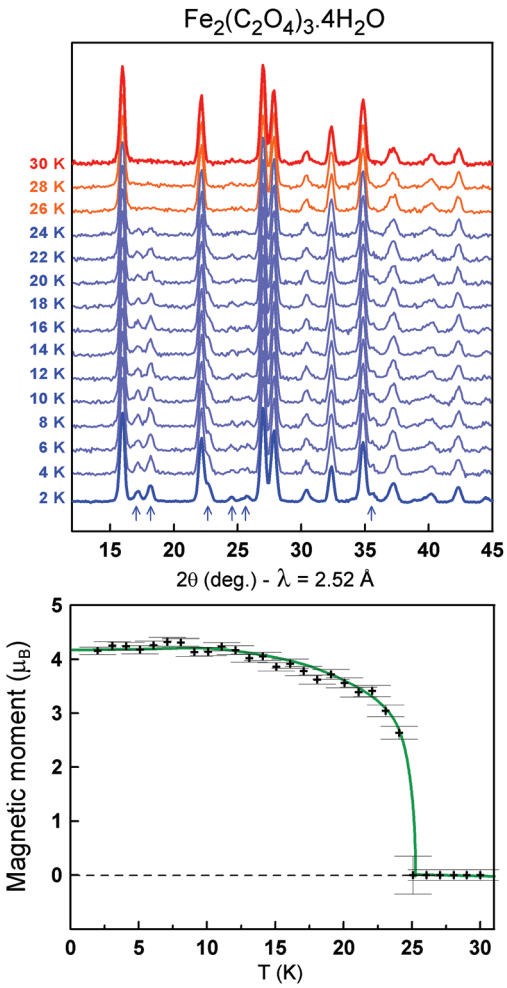

Fig. 3 Neutron diffraction patterns of $Fe_2(C_2O_4)_3{\cdot}4H_2O$ as a function of temperature between 2 K and 30 K (top). The arrows indicate the magnetic reflections appearing under T_N = 25 K. The bottom part shows the dependence of the magnetic moment with temperature, deduced from the Rietveld refinement of the neutron patterns. The green line is a guide to the eye.

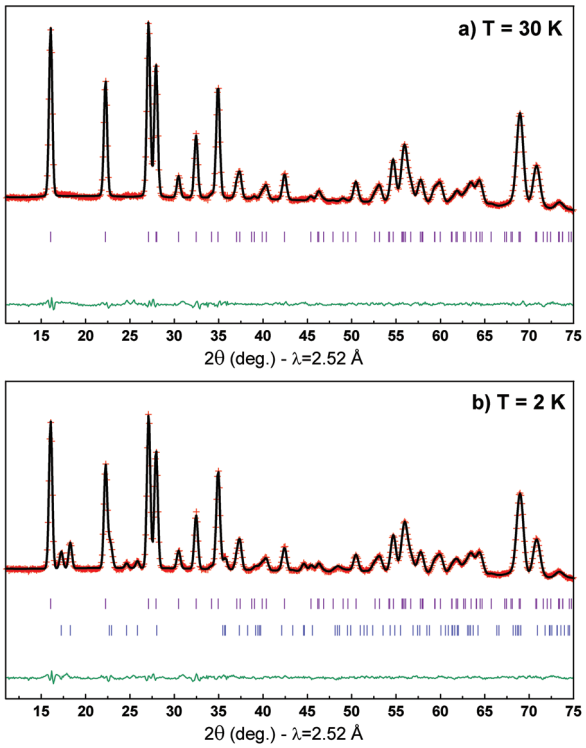

Fig. 4 Rietveld refinement of neutron powder pattern of $Fe_2(C_2O_4)_3{\cdot}4H_2O$ at 30 K, *i.e.* well above the Néel temperature (a) and at 2 K (b). The red crosses, black continuous line and bottom green line represent the observed, calculated, and difference patterns, respectively. Vertical purple and blue tick bars are the Bragg positions of the nuclear and magnetic phases, respectively.

good resolution at a low angle and a large wavelength (λ = 2.52 Å) was chosen to explore low angle magnetic peaks. The powdered sample was placed in a vanadium can and measured from 2 K to 295 K (Fig. 3).

The patterns recorded between 295 K and 30 K are similar to the one expected from the structural model, with only a shift in lattice parameters. The Rietveld refinement of the data collected at 30 K is shown in Fig. 4a and perfectly confirms the structural model reported at room temperature. The triclinic cell (space group $P\bar{1}$) has lattice parameters a = 5.2721(2) Å, b = 6.5439(2) Å, c = 9.0963(3) Å, α = 91.568(2)°, β = 97.293(3)° and γ = 93.097(2)°. The volume V = 310.65(2) Å^3 accommodates one formula unit: a single crystallographic site (general position 2*i*) with two iron atoms per cell. When the temperature further decreases, nuclear peaks remain unchanged (only a shift of peaks with temperature is observed due to thermal expansion), indicating the absence of structural distortion at low temperature. However, we notice below 25 K the appearance of additional diffraction peaks in the neutron powder pattern, as shown in Fig. 3. These extra peaks increase in intensity and reach a maximum when the temperature reaches 2 K. These reflections present therefore characteristics consistent with magnetic peaks arising from a long-range ordering of the magnetic moments carried by Fe^{3+}. At this stage, one should note that the Néel temperature deduced from neutron experiments (25 K) is significantly lower than the maximum of susceptibility (~55 K). Such a discrepancy was already observed in other compounds, such as tavorite $FeSO_4F$,[36] therefore caution should be

Table 1 Results of the Rietveld refinement of the 2 K neutron pattern of $Fe_2(C_2O_4)_3{\cdot}4H_2O$. Structural parameters as well as magnetic moments for Fe are reported (in terms of components along the *a*, *b* and *c* lattice basis vectors and resulting magnitude *M*). Isotropic temperature factors B were constrained identical for a same chemical species, except for O8 which belongs to a water molecule not linked to Fe

Lattice parameters of $Fe_2(C_2O_4)_3{\cdot}4H_2O$ at 2 K:

a = 5.27059(14) Å, b = 6.54165(16) Å, c = 9.09608(18) Å, α = 91.5602(24)°, β = 97.2839(26)°, γ = 93.0821(21)°, V = 310.453(14) Å^3

Atom	Wyckoff site	x	y	z	B (Å^2)
Fe	2*i*	0.4754(13)	0.2876(9)	0.2385(9)	0.92(25)
C1	2*i*	0.125(2)	0.0700(18)	0.0068(16)	0.64(23)
C2	2*i*	0.389(2)	0.4369(17)	0.5233(15)	0.64(23)
C3	2*i*	0.386(2)	0.554(2)	0.0116(16)	0.64(23)
O1	2*i*	0.210(2)	0.154(2)	0.9065(15)	0.01(12)
O2	2*i*	0.233(2)	0.0839(18)	0.1472(13)	0.01(12)
O3	2*i*	0.290(2)	0.3198(18)	0.4183(16)	0.01(12)
O4	2*i*	0.284(2)	0.487(2)	0.6325(19)	0.01(12)
O5	2*i*	0.289(2)	0.513(2)	0.1305(18)	0.01(12)
O6	2*i*	0.712(2)	0.3189(19)	0.0769(12)	0.01(12)
O7	2*i*	0.682(3)	0.077(2)	0.334(2)	0.01(12)
H71	2*i*	0.785(5)	0.111(4)	0.443(3)	2.4(4)
H72	2*i*	0.762(5)	−0.020(4)	0.257(2)	2.4(4)
O8	2*i*	0.156(3)	0.792(3)	0.387(2)	1.2(4)
H81	2*i*	0.194(4)	0.861(4)	0.285(4)	2.4(4)
H82	2*i*	0.017(5)	0.690(3)	0.359(4)	2.4(4)

Magnetic part $\mathbf{k} = (\frac{1}{2}, \frac{1}{2}, 0)$

Atom	Fe in (0.475(2), 0.288(1), 0.239(1))	Fe in (−0.475(2), −0.288(1), −0.239(1))
M_X	1.16(7)μ_B	−1.16(7)μ_B
M_Y	−0.88(12)μ_B	0.88(12)μ_B
M_Z	4.00(4)μ_B	−4.00(4)μ_B
M	4.16(3)μ_B	4.16(3)μ_B

taken to determine T_N from susceptibility curves presenting broad maxima. The magnetic structure was therefore solved from the pattern recorded at 2 K. It appears that these magnetic reflections can be indexed with a propagation vector $\mathbf{k} = (\frac{1}{2}, \frac{1}{2}, 0)$ relative to the nuclear cell. Therefore the magnetic unit cell is four times larger than the nuclear cell.

A symmetry analysis was performed using Bertaut's method[37,38] in order to determine the spin configurations that are compatible with the crystal symmetry of $Fe_2(C_2O_4)_3{\cdot}4H_2O$ with vector $\mathbf{k} = (\frac{1}{2}, \frac{1}{2}, 0)$, and iron moments carried by Fe^{3+} in the $2i$ site of $P\bar{1}$ with $x = 0.475(2)$, $y = 0.288(1)$ and $z = 0.239(1)$.

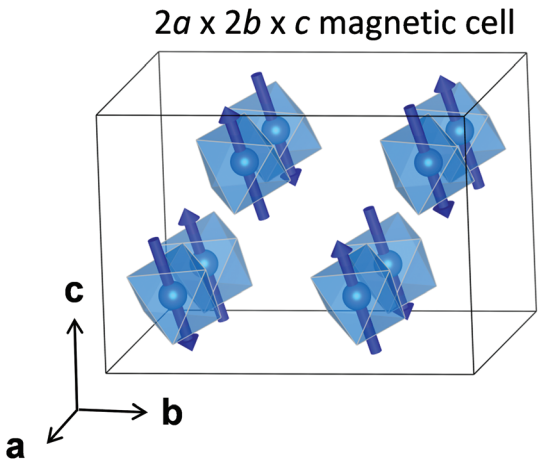

Fig. 5 Magnetic structure of $Fe_2(C_2O_4)_3{\cdot}4H_2O$. Blue arrows represent magnetic moments carried by the Fe^{3+} atoms. The magnetic structure is represented in the $2a \times 2b \times c$ magnetic cell (a, b, c refer to the nuclear cell). For the sake of clarity, non-magnetic atoms are not represented.

The magnetic representation Γ_{magn} can be trivially decomposed upon two irreducible representations Γ_1 and Γ_2, each with three basis vectors collinear to one crystal axis: $\Gamma_{magn} = 3\Gamma_1 + 3\Gamma_2$. Γ_1 (resp. Γ_2) corresponds to a parallel (resp. antiparallel) coupling between magnetic moments carried by iron at x, y, z and $-x$, $-y$, $-z$ in the paramagnetic cell. Symmetry allows only collinear structures with a net resultant magnetization equal to zero because $\mathbf{k} = (\frac{1}{2}, \frac{1}{2}, 0)$, there is no constraint in the direction of the magnetic moment because in triclinic space groups there is only the identity or the centre of symmetry in atom positions.

The best agreement was obtained using the Γ_2 irreducible representation, with magnetic moments having components along the three crystallographic directions, as reported in Table 1. The largest component is directed along [001] ($M_z = 4.00(4)\mu_B$), with components of $1.16(7)\mu_B$ and $-0.88(12)\mu_B$ along [100] and [010], respectively. This corresponds to a moment magnitude of $4.16(3)\mu_B$, consistent with the value expected for a Fe^{3+} ion. The Rietveld refinement of the pattern recorded at 2 K is shown in Fig. 4b. The refinement was also done using the magnetic space group description, with the Shubnikov group $P_s\bar{1}$, in the quadruple magnetic cell $2a \times 2b \times c$ (with a, b and c lattice basis vectors for the nuclear cell). This gave exactly the same refinement and magnetic structure as the approach explained before with the propagation vector. The magnetic cif file (*.mcif) obtained from the refinement at 2 K is given in the ESI.† Fig. 5 shows the obtained magnetic structure in the $2a \times 2b \times c$ magnetic cell.

Lastly, all neutron patterns between 2 K and 30 K can be refined using this antiferromagnetic structure; the resulting temperature dependence of the magnetic moment is given in the bottom part of Fig. 3, and fully confirms 25 K as the Néel temperature.

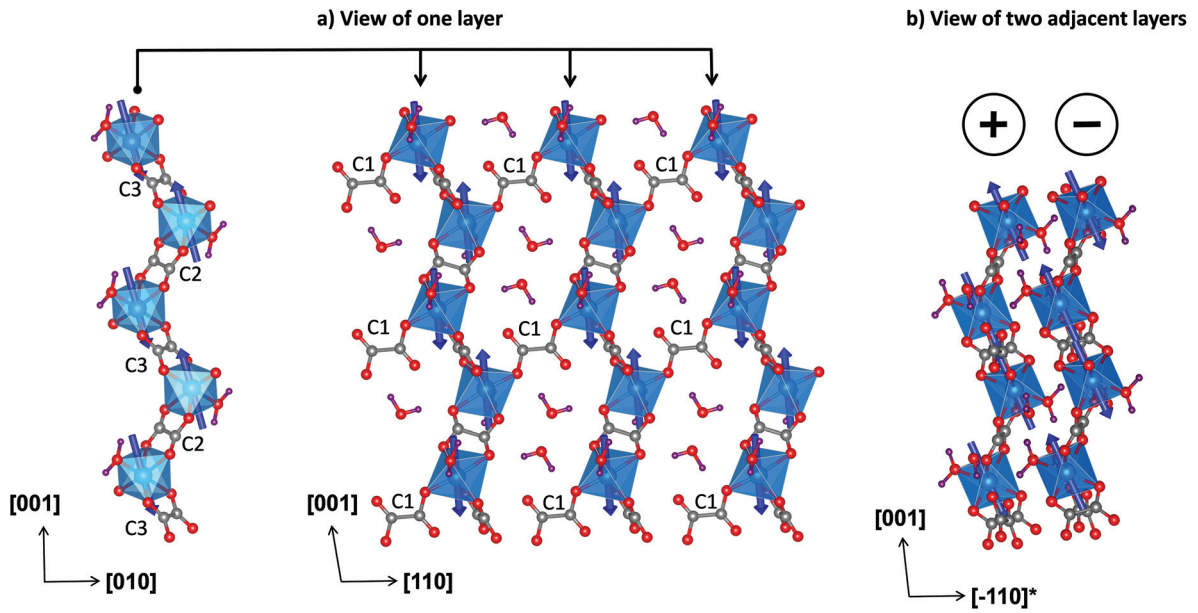

Fig. 6 Magnetic structure of $Fe_2(C_2O_4)_3{\cdot}4H_2O$. Blue arrows represent magnetic moments carried by the Fe^{3+} atoms. (a) View of one Fe-oxalate layer (b) view showing two adjacent Fe-oxalate layers.

Analysis of the magnetic structure

Let us now examine the manner magnetic moments are coupled through the oxalate ligands. The structure of $Fe_2(C_2O_4)_3{\cdot}4H_2O$ can be regarded as formed of corrugated layers obtained by connecting iron atoms and oxalate groups. These layers are stacked along [1, −1, 0]* and are not chemically connected (no chemical bond in between). Each layer is composed of FeO_6 octahedra linked to each other through oxalate groups: the two tetradentate oxalate groups (built on carbon atoms C2 and C3) form Fe-ox-Fe chains and the third oxalate group (built on C1) links adjacent chains in a *trans* configuration. A view of a single layer is shown in Fig. 6a. The three crystallographically-distinct oxalate groups (built on C1, C2 and C3 respectively) mediate different couplings that all generate an antiparallel arrangement of adjacent magnetic moments, as seen in Fig. 7. Overall, four exchange integrals should be taken into account: J_1 and J_2 are the shortest ones, with Fe–Fe distances of 5.242(12) Å and 5.414(12) Å, respectively. They both connect Fe atoms, *via* a tetradentate oxalate

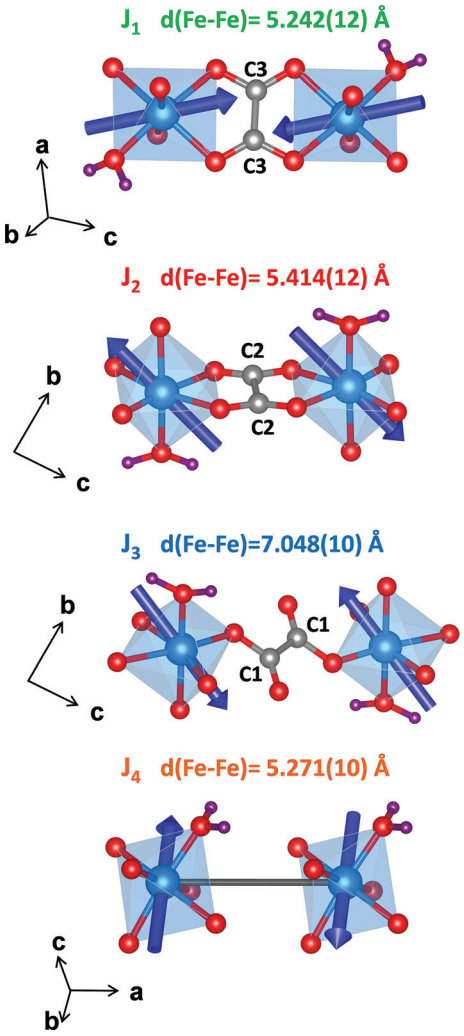

Fig. 7 Illustration of the four magnetic exchange paths present in the structure and the relative orientation of the Fe^{3+} magnetic moments.

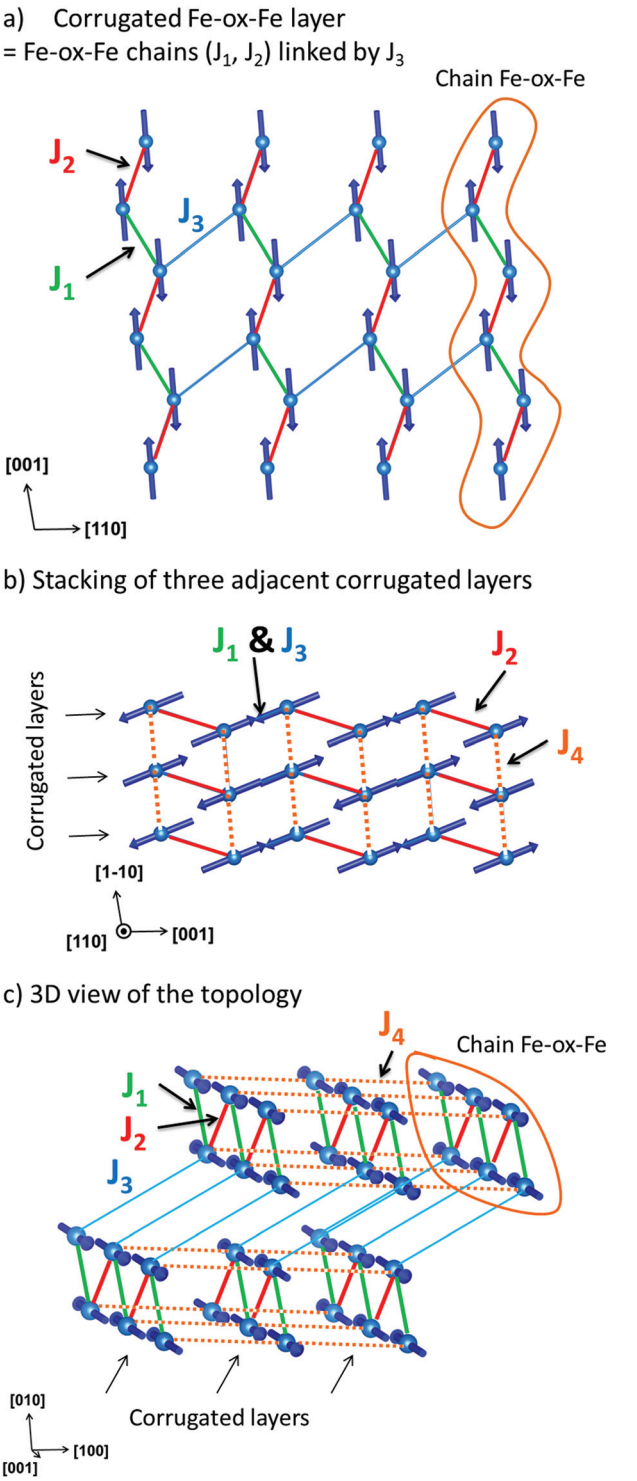

Fig. 8 Topology of the magnetic structure of $Fe_2(C_2O_4)_3{\cdot}4H_2O$. Only Fe atoms are represented and the arrows represent the magnetic moments. J_1 and J_2 (tetradentate oxalate) form Fe-ox-Fe chains linked by a *trans* oxalate (J_3) to form a corrugated layer (a). This leads to 6-leg hexagons. J_4 connects two adjacent corrugated layers (b). (c) Shows a tri-dimensional view of the topology. In this view, the corrugated Fe-ox-Fe layers appear tilted by about 45°.

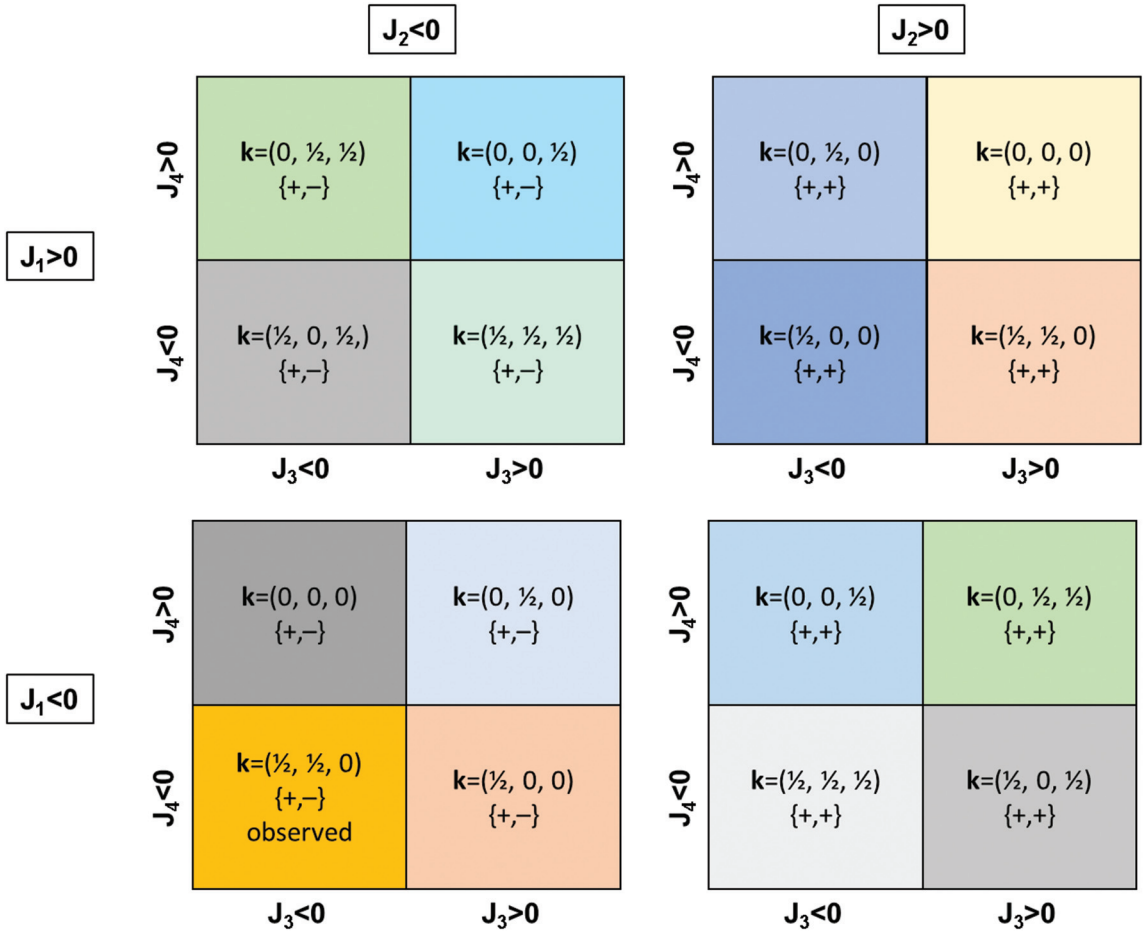

Fig. 9 Phase diagrams showing the influence of the sign of the super–super-exchange integrals J_1, J_2, J_3 and J_4 on the possible ground-state magnetic structures of $Fe_2(C_2O_4)_3{\cdot}4H_2O$. Sign sequences correspond to the magnetic moments carried by the two iron atoms belonging to the Wyckoff site 2*i*. The magnetic structure experimentally observed (*i.e.* deduced from the neutron diffraction experiment at 2 K) corresponds to $J_1 < 0$, $J_2 < 0$, $J_3 < 0$ and $J_4 < 0$ (orange domain).

group. The third one, J_3, connects two Fe atoms (d(Fe–Fe) = 7.048(10) Å) *via* a bidentate oxalate group in a *trans* configuration. J_1 and J_2 create Fe-ox-Fe chains while J_3 connects chains to an adjacent one, so as to form the corrugated layers mentioned above with a topology that presents 6-leg polygons (Fig. 8a). J_4 is the shortest distance interaction between Fe-atoms not implying an oxalate group, and links two iron atoms with a distance of 5.271(10) Å (Fig. 8b). J_4 is a long range exchange interaction connecting two successive layers and allowing 3D ordering. A general tri-dimensional view of the topology is given in Fig. 8c. It can be seen that this arrangement does not lead to any frustration, in agreement with the $|\theta_{CW}/T_N|$ ratio of 4. The J_1 and J_2 interactions form Fe-ox-Fe chains and should be responsible for the low-dimensionality behaviour in the susceptibility. J_3 and J_4 are expected to be stronger than J_1 and J_2, but are necessary to establish a long-range 3D ordering of spins as observed from neutron diffraction.

For the sake of completion, a phase diagram of the first ordered state has been calculated using the program EnerMag[39] following a method explained in other papers.[40–43] We obtained 16 different magnetic structures that differ in the propagation vector and the spin sequence of the two iron atoms of the unit cell (Fig. 9). The experimental observed structure, $\mathbf{k} = (\frac{1}{2}, \frac{1}{2}, 0)$ {+, –}, is obtained as a ground state only when all exchange interactions are strictly negative (AF coupling).

Conclusion

Using magnetization measurements and neutron powder diffraction, we have explored and solved the magnetic structure of $Fe_2(C_2O_4)_3{\cdot}4H_2O$ whose structure was elucidated only recently. This compound presents three oxalate-mediated interactions: two tetradentate and one bidentate, and a fourth one which does not correspond to a simple super–super-exchange path. All these interactions should be negative to lead to the observed antiferromagnetic structure. These results highlight that compounds based on the isotropic d^5 Fe^{3+} cation are

prone to generate antiferromagnetic interactions, whatever the nature and geometry of the exchange paths.

Acknowledgements

The authors thank Hania Ahouari for providing the sample, Nadir Recham and Jean-Marie Tarascon for fruitful discussions, and ILL for the neutron beamtime. GR also acknowledges the low temperature platform of the Physics department at UPMC.

References

1 *From Molecular to Supramolecular Chemistry*, ed. J.-M. Lehn, VCH, New York, NY, 2006.
2 G. Givaja, P. Amo-Ochoa, C. J. Gómez-García and F. Zamora, *Chem. Soc. Rev.*, 2012, **41**, 115–147.
3 S. Kitagawa, R. Kitaura and S. Noro, *Angew. Chem., Int. Ed.*, 2004, **43**, 2334–2375.
4 G. Férey, *Chem. Soc. Rev.*, 2008, **37**, 191–214.
5 O. M. Yaghi, M. O'Keeffe, N. W. Ockwig, H. K. Chae, M. Eddaoudi and J. Kim, *Nature*, 2003, **423**, 705–714.
6 M. Verdaguer, *Science*, 1996, **272**, 698.
7 O. Kahn, *Molecular Magnetism*, Wiley-VCH, New York, NY, 1st edn, 1993.
8 C. Ruiz-Pérez, Y. Rodríguez-Martín, M. Hernández-Molina, F. S. Delgado, J. Pasán, J. Sanchiz, F. Lloret and M. Julve, *Polyhedron*, 2003, **22**, 2111–2123.
9 Z. Wang, K. Hu, S. Gao and H. Kobayashi, *Adv. Mater.*, 2010, **22**, 1526–1533.
10 M. Liang, Q.-L. Wang, L.-H. Yu, D.-Z. Liao, Z.-H. Jiang, S.-P. Yan and P. Cheng, *Polyhedron*, 2004, **23**, 2203–2208.
11 J. Pasán, F. S. Delgado, Y. Rodríguez-Martín, M. Hernández-Molina, C. Ruiz-Pérez, J. Sanchiz, F. Lloret and M. Julve, *Polyhedron*, 2003, **22**, 2143–2153.
12 F. S. Delgado, C. A. Jiménez, P. Lorenzo-Luis, J. Pasán, O. Fabelo, L. Cañadillas-Delgado, F. Lloret, M. Julve and C. Ruiz-Pérez, *Cryst. Growth Des.*, 2012, **12**, 599–614.
13 F. Su, L. Lu, S. Feng, M. Zhu, Z. Gao and Y. Dong, *Dalton Trans.*, 2015, **44**, 7213–7222.
14 E. Colacio, J. M. Dominguez-Vera, M. Ghazi, R. Kivekäs, M. Klinga and J. M. Moreno, *Eur. J. Inorg. Chem.*, 1999, 441–446.
15 F. S. Delgado, J. Sanchiz, C. Ruiz-Pérez, F. Lloret and M. Julve, *Inorg. Chem.*, 2003, **42**, 5938–5948.
16 I. G. de Muro, M. Insausti, L. Lezama, M. K. Urtiaga, M. I. Arriortua and T. Rojo, *J. Chem. Soc., Dalton Trans.*, 2000, 3360–3364.
17 I. Gil de Muro, L. Lezama, M. Insausti and T. Rojo, *Eur. J. Inorg. Chem.*, 2003, **2003**, 2948–2954.
18 Y. Rodríguez-Martín, M. Hernández-Molina, J. Sanchiz, C. Ruiz-Pérez, F. Lloret and M. Julve, *Dalton Trans.*, 2003, 2359–2365.
19 T. K. Maji, S. Sain, G. Mostafa, T.-H. Lu, J. Ribas, M. Monfort and N. R. Chaudhuri, *Inorg. Chem.*, 2003, **42**, 709–716.
20 I. G. de Muro, F. A. Mautner, M. Insausti, L. Lezama, M. I. Arriortua and T. Rojo, *Inorg. Chem.*, 1998, **37**, 3243–3251.
21 L. Cañadillas-Delgado, O. Fabelo, J. A. Rodríguez-Velamazán, M.-H. Lemée-Cailleau, S. A. Mason, E. Pardo, F. Lloret, J.-P. Zhao, X.-H. Bu, V. Simonet, C. V. Colin and J. Rodríguez-Carvajal, *J. Am. Chem. Soc.*, 2012, **134**, 19772–19781.
22 O. Fabelo, L. Cañadillas-Delgado, J. Pasán, F. S. Delgado, F. Lloret, J. Cano, M. Julve and C. Ruiz-Pérez, *Inorg. Chem.*, 2009, **48**, 11342–11351.
23 C. Mennerich, H. H. Klauss, M. Broekelmann, F. J. Litterst, C. Golze, R. Klingeler, V. Kataev, B. Buechner, S. N. Grossjohann, W. Brenig, M. Goiran, H. Rakoto, J. M. Broto, O. Kataeva and D. J. Price, *Phys. Rev. B: Condens. Matter*, 2006, **73**, 174415.
24 C. Mennerich, H. H. Klauss, A. U. B. Wolter, S. Sullow, F. J. Litterst, C. Golze, R. Klingeler, V. Kataev, B. Buchner, M. Goiran, H. Rakoto, J. M. Broto, O. Kataeva and D. J. Price, in *Quantum Magnetism*, ed. B. Barbara, Y. Imry, G. Sawatzky and P. C. E. Stamp, 2008, pp. 97–124.
25 S. Decurtins, R. Pellaux, G. Antorrena and F. Palacio, *Coord. Chem. Rev.*, 1999, **190**, 841–854.
26 M. B. Hursthouse, M. E. Light and D. J. Price, *Angew. Chem., Int. Ed.*, 2004, **43**, 472–475.
27 J. Glerup, P. A. Goodson, D. J. Hodgson and K. Michelsen, *Inorg. Chem.*, 1995, **34**, 6255–6264.
28 N. Marino, D. Armentano, G. De Munno, F. Lloret, J. Cano and M. Julve, *Dalton Trans.*, 2015, **44**, 11040–11051.
29 D. Armentano, G. de Munno, F. Lloret, M. Julve, J. Curély, A. M. Babb and J. Y. Lu, *New J. Chem.*, 2003, **27**, 161–165.
30 C. Mathonière, C. J. Nuttall, S. G. Carling and P. Day, *Inorg. Chem.*, 1996, **35**, 1201–1206.
31 H. Ahouari, G. Rousse, J. Rodríguez-Carvajal, M.-T. Sougrati, M. Saubanère, M. Courty, N. Recham and J.-M. Tarascon, *Chem. Mater.*, 2015, **27**, 1631–1639.
32 H. M. Rietveld, *J. Appl. Crystallogr.*, 1969, **2**, 65–71.
33 J. Rodríguez-Carvajal, *Physica B*, 1993, **192**, 55–69.
34 J. Rodríguez-Carvajal, *FullProf Suite*, http://www.ill.eu/sites/fullprof/.
35 F. E. Mabbs and D. J. Machin, *Magnetism and Transition Metal Complexes*, Dover Publications, Mineola, NY, 2008.
36 B. C. Melot, G. Rousse, J. N. Chotard, M. Ati, J. Rodriguez-Carvajal, M. C. Kemei and J. M. Tarascon, *Chem. Mater.*, 2011, **23**, 2922–2930.
37 E. F. Bertaut, *Acta Crystallogr., Sect. A: Cryst. Phys., Diffr., Theor. Gen. Cryst.*, 1968, **24**, 217–231.
38 E. F. Bertaut, *J. Phys. Colloques*, 1971, **32**, C1-462–C1-470.
39 J. Rodríguez-Carvajal, *SIMBO, ENERMAG and PHASE_DIAGRAM programs, available within the examples of the CrysFML repository*, available at https://forge.epn-campus.eu/projects/crysfml/repository/show/Program_Examples.

40 G. Rousse, J. Rodriguez-Carvajal, S. Patoux and C. Masquelier, *Chem. Mater.*, 2003, **15**, 4082–4090.
41 G. Rousse, J. Rodríguez-Carvajal, C. Wurm and C. Masquelier, *Phys. Rev. B: Condens. Matter*, 2013, **88**, 214433.
42 M. Reynaud, G. Rousse, J.-N. Chotard, J. Rodríguez-Carvajal and J.-M. Tarascon, *Inorg. Chem.*, 2013, **52**, 10456–10466.
43 M. Reynaud, J. Rodríguez-Carvajal, J.-N. Chotard, J.-M. Tarascon and G. Rousse, *Phys. Rev. B: Condens. Matter*, 2014, **89**, 104419.